crystals

MDPI

Article

Regulation of the Thermoelectric Properties of Perovskite $RECoO_3$ Ceramics via High-Entropy Engineering

Kezhen Zhang, Chengchao Yang, Xianpeng Ao, Yulong Zhao, Weihao Tan, Jinglong Wu, Bin Liu *, Kun Dong, Liangwei Chen and Lan Yu *

Faculty of Materials Science and Engineering, Kunming University of Science and Technology, Kunming 650000, China; 20222230208@stu.kust.edu.cn (K.Z.); yangcc_cc@163.com (C.Y.); 20222230041@stu.kust.edu.cn (X.A.); 20232130020@stu.kust.edu.cn (Y.Z.); 20232130006@stu.kust.edu.cn (W.T.); 20242230081@stu.kust.edu.cn (J.W.); dongkun3000@foxmail.com (K.D.); elegantbaby@126.com (L.C.)

* Correspondence: bliu0201@foxmail.com (B.L.); yulan000@hotmail.com (L.Y.)

Abstract: Entropy engineering has been demonstrated to be an effective strategy to regulate the thermoelectric properties of materials. In this work, we report a series of single-phase cubic $(La_{0.25}Sr_{0.25}Ba_{0.25}Ca_{0.25})CoO_3$ (LSBC), $(La_{0.25}Nd_{0.25}Sr_{0.25}Ba_{0.25})CoO_3$ (LNSB), and $(La_{0.2}Nd_{0.2}Sr_{0.2}Ba_{0.2}Ca_{0.2})CoO_3$ (LNSBC) ceramics based on high-entropy design in the Re site of perovskite $RECoO_3$. Electron microscopy results indicate that the three samples have high crystallinity and exhibit a clear pore structure with rich lattice defects. Electrical transport measurements show that LNSB and LNSBC show metallic conductive behaviors with the lowest resistivity of only 2.25 mΩ cm at 973 K, while LSBC exhibits a semiconductor–metal transition at around 650 K due to the lower average chemical valences in the RE site. Meanwhile, the low average chemical valences also cause the increasing proportion of Co^{4+} due to the requirement of charge neutrality of the samples, which inhibits their Seebeck coefficients. However, compared with the reported Co-based perovskite oxides, their thermal conductivities are greatly reduced owing to high-entropy enhanced lattice scattering. LSBC in particular obtains the lowest thermal conductivity of 1.25 $W \cdot m^{-1} \cdot K^{-1}$ at 937 K, while LNSB and LNSBC characterized by high carrier thermal conductivity exhibit a thermal conductivity of 1.52 $W \cdot m^{-1} \cdot K^{-1}$ at the same temperature. These findings reveal that high-entropy design in the RE site of perovskite $RECoO_3$ ceramics enables the effective reduction of thermal conductivity and the maintenance of the excellent electrical properties simultaneously, which provides a novel route for the development of high-performance thermoelectric materials.

Keywords: co-based perovskite oxides; entropy engineering; thermoelectric property; high-entropy design; thermal conductivity

check for updates

Academic Editor: Francisco M. Morales

Received: 26 February 2025
Revised: 9 March 2025
Accepted: 11 March 2025
Published: 20 March 2025

Citation: Zhang, K.; Yang, C.; Ao, X.; Zhao, Y.; Tan, W.; Wu, J.; Liu, B.; Dong, K.; Chen, L.; Yu, L. Regulation of the Thermoelectric Properties of Perovskite $RECoO_3$ Ceramics via High-Entropy Engineering. *Crystals* **2025**, *15*, 285. https://doi.org/10.3390/cryst15030285

Copyright: © 2025 by the authors. Licensee MDPI, Basel, Switzerland. This article is an open access article distributed under the terms and conditions of the Creative Commons Attribution (CC BY) license (https://creativecommons.org/licenses/by/4.0/).

1. Introduction

Thermoelectric (TE) materials can directly and reversibly convert exhaust heat to electrical energy without environmental pollution, showing great potential in the development of sustainable and clean energy [1–3]. In general, the conversion efficiency of TE materials is evaluated from a dimensionless figure of merit (ZT), namely, $ZT = (S^2 \cdot \sigma \cdot T)/\kappa$, where S is the Seebeck coefficient, σ is the electrical conductivity, T is the absolute temperature, and κ is the thermal conductivity. It can thus be seen that desirable TE performance requires high electrical conductivity, a large Seebeck coefficient, and low thermal conductivity, but due to the strong coupling interaction between them, it remains challenging to develop high-performance TE materials [4–6].

In this regard, an effective practice is to design a TE material with a phonon–glass electron–crystal nature, in which the electron–crystal maintains the excellent electrical properties of the stable crystal structure and regular band structure, while the phonon glass lowers the lattice thermal conductivity through enhanced phonon scattering due to the locally disordered atomic occupancy [7,8]. Cubic perovskite oxide $RECoO_3$ (RE = rare earth) is a promising candidate for constructing phonon–glass electron–crystal-type TE materials because of its unique structural features, with it containing the order Co site and disorder RE site simultaneously [9,10], which is beneficial for the regulation of TE properties. However, their high thermal conductivity and relatively low electrical conductivity at room temperature are still the main obstacles to their further development [11]. In the past few years, many efforts have been made to improve TE performance, including chemical doping or atomic substitution in the RE site [12,13], Co site [14,15], and dual site [16,17], nano-structuring [18], hot-pressing sintering [19], spark plasma sintering [20], and so on. For instance, Wang et al. reported an improvement in the TE properties of $LaCoO_3$ by replacing La with Sr/Ca to decrease its thermal conductivity [12]. Kumar A. et al. obtained a ZT value of 0.14 at 480 K by regulating the spin temperature from Sr and Mn dually doped $LaCoO_3$ [16]. However, the coupling relationship between the electrical and thermal parameters of $RECoO_3$ results in unbalanced electrical and thermal natures, and more effective strategies are highly required to improve TE performance.

Recently, high-entropy alloys, which are defined as single-phase solid solution alloys that contain four or more principal elements in equal or near equal atomic percent (at. %) [21–24], have been widely used to design advanced TE materials [25–29]. High-entropy-driven structural stabilization enables the enhancement of electrical properties [26,30]. Meanwhile, the induced lattice distortion or structural defects can also intensify lattice scattering and reduce the thermal conductivity effectively [31]. For example, Gao et al. developed a $Sr_{0.9}La_{0.1}(Zr_{0.25}Sn_{0.25}Ti_{0.25}Hf_{0.25})O_3$ high-entropy sample by adding four transition metal elements onto the Co site and achieved a low thermal conductivity of 1.89 W/m/K and a high Seebeck coefficient of 393 μV/K at 873 K [17], indicating that the high-entropy concept is a promising method to explore novel perovskite oxide TE materials. However, there are few reports about high-entropy design at RE sites in Co-based perovskite oxides; in particular, the effects of mixing entropy on TE properties are unclear. In this work, we adopted a selective high-entropy design by introducing multiple cations into the RE site of the perovskite $RECoO_3$ ceramic, aiming to enhance the electrical properties and decrease the thermal conductivity simultaneously. A series of high-entropy perovskite ceramics $RECoO_3$ (RE = La, Nd, Ca, Sr, Ba) were thus obtained, namely $(La_{0.25}Sr_{0.25}Ba_{0.25}Ca_{0.25})CoO_3$ (LSBC), $(La_{0.25}Nd_{0.25}Sr_{0.25}Ba_{0.25})CoO_3$ (LNSB), and $(La_{0.2}Nd_{0.2}Sr_{0.2}Ba_{0.2}Ca_{0.2})CoO_3$ (LNSBC). Indeed, such partial high-entropy design endows them with high electrical conductivities because of the unbroken long-range order of this highly symmetrical cubic structure. Additionally, the three samples exhibit low thermal conductivity (1.32–1.55 $W \cdot m^{-1} \cdot K^{-1}$) due to the various scattering centers derived from the short-range disordered atomic arrangement in high-entropy RE site cations. This work provides a good illustration of high-entropy effects on the regulation of electrical and thermal transport properties as well as the improvement of TE performance in perovskite oxides. Also, these results demonstrate that adopting high-entropy engineering to decouple the contradiction between the TE parameters is a truly effective strategy to improve TE performance.

2. Materials and Methods

High-entropy oxide ceramics, LSBC, LNSB, and LNSBC, were prepared using a conventional solid-state reaction. Firstly, the powders of the raw chemicals La_2O_3, Nd_2O_3,

$SrCO_3$, $BaCO_3$, $CaCO_3$, and Co_3O_4 were weighted based on the chemical stoichiometric ratio and then fully mixed. Afterward, the well-mixed powders were pressed into tablets and transferred to a muffle furnace for sintering at 910 °C for 24 h in air. Secondly, the preliminarily sintered samples were thoroughly ground into powder, which was pressed into pellets. Finally, these samples were cooled to room temperature after being annealed at 1100 °C for 24 h under air. In addition, the prepared ceramics were further processed into different shapes with suitable sizes for various physical property measurements.

The crystal structures of the samples were confirmed using X-ray diffraction (XRD, Rigaku MiniFex, Japan) with Cu Kα radiation. The surface morphology and chemical composition were investigated using a Scanning Electron Microscope (SEM, Tescan-VEGA3, Czech Republic) equipped with an energy-dispersive spectrometer (EDS). The microstructures of the samples were studied using a transmission electron microscope (TEM, FEI-Tecnai G2 F30S-Twin, USA), in which the sample was ultrasonically dispersed in ethanol solution and loaded on a copper mesh to observe the lattice fringes and multi-scale structural defects. Moreover, the interplanar crystal spacing and selected electron diffraction (SAED) were observed and analyzed with Digital Micrograph 3.4 software. The chemical valences were measured via X-ray photoelectron spectroscopy with Al Kα radiation (XPS, PHI5000 VersaProbe III, Japan). The Seebeck coefficient and electrical conductivity were tested on a TE testing system, and the sample was treated with a size of 12 mm × 3 mm× 3 mm (LSR-3/1100, Linseis, Germany). The diffusion coefficient (D) was measured by means of the laser flash technique (LFA- 457, Netzsch, Germany), and the thermal conductivity was estimated from the formula: $\kappa = \rho_D D C_p$, where the density (ρ_D) was obtained using the Archimedes principle and the heat capacity (C_p) was calculated from the temperature-independent Dulong–Petit rule. The carrier concentration (n) and mobility (μ_H) at room temperature were obtained using Hall effect measurement (HMS-7000, Ecopia, Republic of Korea) at a magnetic field of 0.5 T.

3. Results and Discussion

3.1. XRD Analysis

Figure 1a shows the XRD patterns of the three high-entropy $RECoO_3$ ceramics. They exhibit a typical set of cubic perovskite crystal diffraction peaks, with no other impurity peaks being observed, which are well indexed on a cubic lattice with a space group of $Pm\bar{3}m$, implying that multiple cations are introduced into the RE site of the lattice to form a single-phase solid solution [8,32]. Figure 1b shows a magnified view of the main (110) diffraction peak. Due to the various ionic radii in the RE site, the lattice constant (a) of the sample decreases with the decreasing average ionic radius of the RE site ($R_{LSBC} > R_{LNSB} > R_{LNSBC}$), which results in the gradual shift of the diffraction peak (110) to a higher angle. Moreover, to further determine the crystal structure of the $RECoO_3$ ceramics, we performed Rietveld refinement based on GSAS II software. As displayed in Figure 1b–d, the refined XRD patterns of the three samples are in good agreement with the experimental results with small Rietveld refinement factors (R_{wp} and χ^2), confirming the reliability and correction of the refined results. The lattice constants of LSBC, LNSB, and LNSBC are calculated as 3.8795(4) Å, 3.8596(2) Å, and 3.8320(5) Å, respectively, which is consistent with the average ionic radius in the RE site. These related lattice parameters are summarized in Table 1.

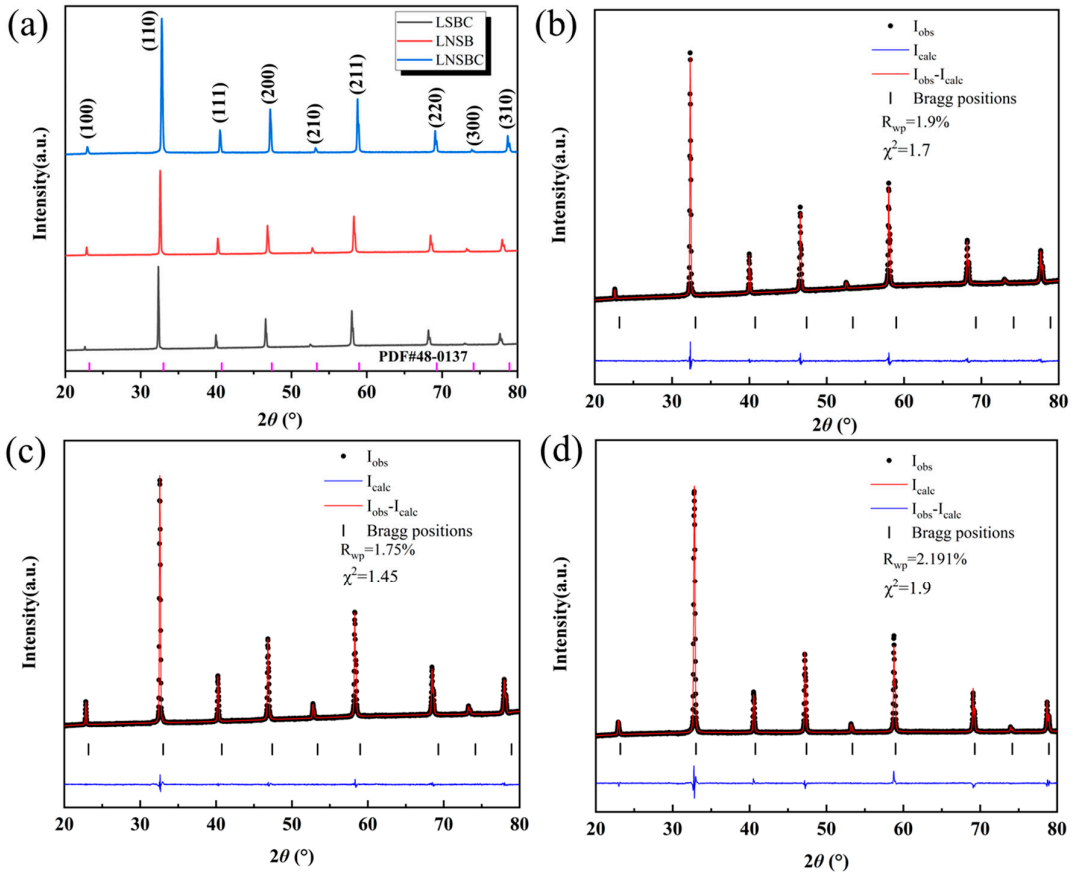


Figure 1. (**a**) XRD patterns of the high-entropy $RECoO_3$ ceramics and the structural refinement profiles of (**b**) LSBC, (**c**) LNSB, and (**d**) LNSBC.

Table 1. Lattice parameters and TE properties of the high-entropy $RECoO_3$ ceramics.

Parameter	LSBC	LNSB	LNSBC
a (Å)	3.8795(4)	3.8596(2)	3.8320(5)
α, β, γ (°)	90	90	90
R_{wp} (%)	1.9	1.75	2.19
χ^2	1.7	1.45	1.9
V_{RE}	2.25	2.5	2.4
ρ_D (g·cm^3)	4.36	4.34	4.49
n (10^{20} cm^{-3})	1.06	6.70	3.57
μ_H (cm^2·V^{-1}·s^{-1})	45.0	16.3	28.8
R_H (cm^3·C^{-1})	5.9×10^{-2}	9.32×10^{-3}	1.7×10^{-2}
ρ_T = 300 K (mΩ·cm)	14.5	0.53	0.58
S_{max} (μV·K^{-1})	27	6.3	8.7
PF_{max} (μW·m^{-1}·K^{-2})	5.5	1.8	3.2
$\kappa_{tot,min}$ (W·m^{-1}·K^{-1})	1.27	1.56	1.54

3.2. Microstructure and Composition Analysis

Figure 2a–c shows the SEM-BSE images of the three high-entropy $RECoO_3$ ceramics. LSBC, LNSB and LNSBC display good crystallinity, and the grain boundaries are connected to one another to form a porous structure. LSBC has a larger grain size of about 20 μm, while LNSB has the smallest grain size of 1–5 μm, with the grain size of LNSBC being between them. We conclude that the introduction of smaller Ca^{2+} makes it easier for LNSBC to diffuse, compared with La^{3+}, Nd^{3+}, Sr^{2+}, and Ba^{2+} ions, which contributes to the grain growth and quick bonding during the sintering process [33]. Moreover, the backscatter

BSE signals suggest that the compositions of the three samples are evenly distributed without phase segregation, which can also be supported by the EDS results. As described in Figure 2d, each element distributes uniformly in the LNSBC sample, and no element aggregation and segregation are observed. The atomic ratios of each element in the RE site are close to 1:1, further confirming that LNSBC is a single-phase solid solution.

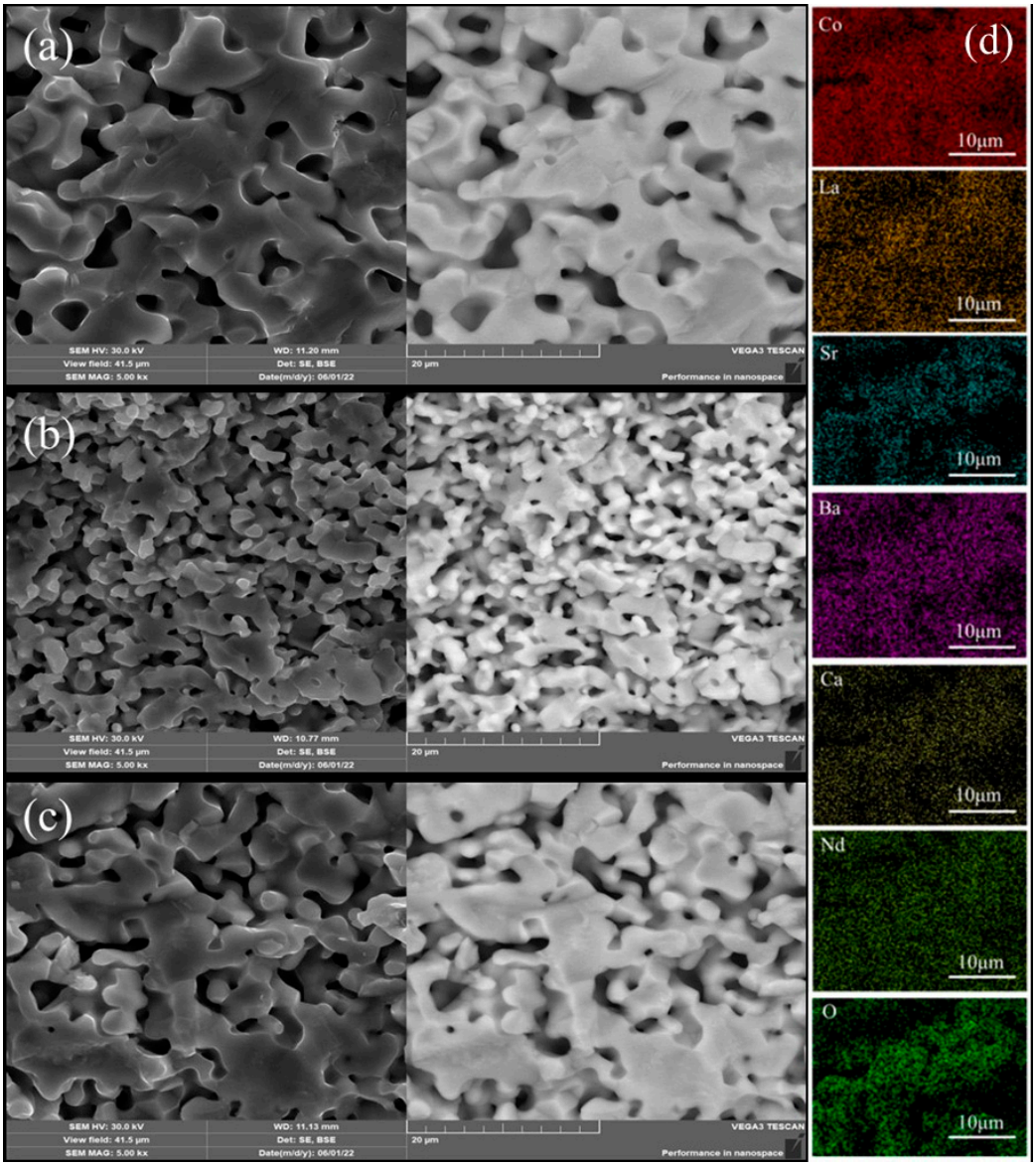


Figure 2. SEM-BSE images of (**a**) LSBC, (**b**) LNSB, (**c**) and LNSBC. (**d**) Elemental distribution of the LNSBC sample determined through EDS measurement.

We further analyzed the microstructures using the TEM measurements. Figure 3a presents the high-resolution TEM mappings of the representative LNSBC sample, which displays an apparent lamellar structure. The selective electron diffraction (SAED) illustrated in Figure 3b reflects the cubic structure of the sample. Moreover, some weak diffraction spots in the superstructure are also observed, which is probably because the occurrence of oxygen octahedral in-phase rotation and the reverse displacement of the cation, which is consistent with the results of previous studies [17]. Such a superstructure indicates that the LNSBC with RE site short-range disorder forms a long-range ordered solid solution in the entire structure, which can induce a positive effect on the electrical properties. The HRTEM images (Figure 3c,d) show the high-quality crystallinity of the sample and the clear

lattice fringe, and the interplanar spacing of (110) is estimated to be 0.2709 nm, effectively matching the theoretical value (0.27099 nm) obtained from the standard PDF card (PDF#48-0137) [34]. The fast Fourier transform (FFT) patterns go along the [111] crystallographic zone axis (Figure 3e) and [0$\bar{1}\bar{1}$] crystallographic zone axis (Figure 3e) of region A, further confirming the cubic structure of the LNSBC. In addition, the corresponding inverse FFT patterns in yellow regions B and C are shown in Figure 3g,h, respectively, with them exhibiting obvious lattice distortion and dislocations. This short-range lattice disorder induced by the multi-component cations in the RE site can effectively scatter low-frequency phonons and inhibit lattice thermal conductivity [35].

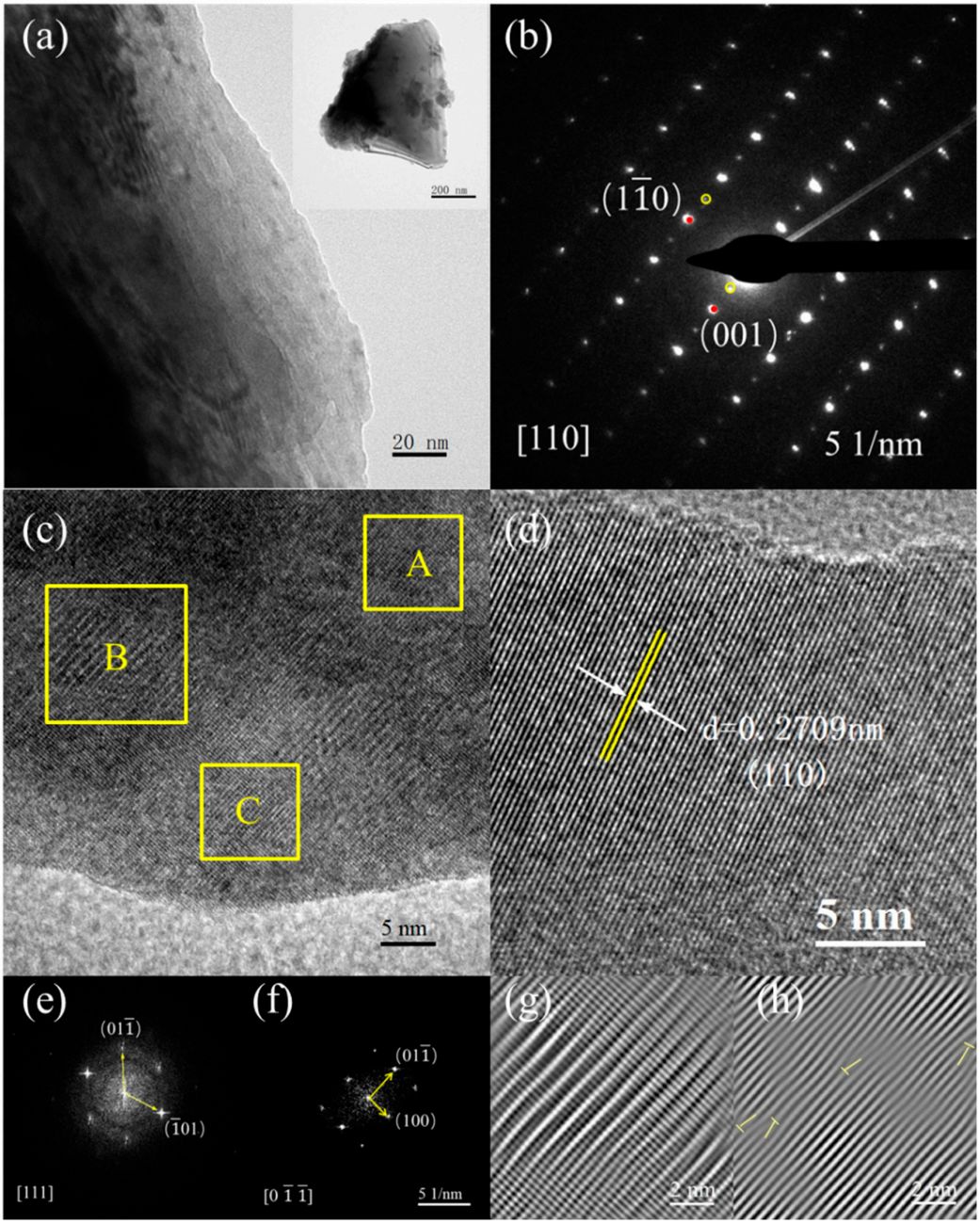


Figure 3. Microstructure characteristics of the LNSBC ceramic. (**a**) TEM bright-field imaging and (**b**) SAED image. (**c**,**d**) High-resolution TEM mappings, and the interplanar spacing of (110) is estimated. (**e**) FFT image along the [111] crystal zone axis in region A. (**f**) FFT image along the [0$\bar{1}\bar{1}$] crystal zone axis in region A. (**g**) Layer dislocation image in region B. (**h**) Dislocation image in region C.

3.3. Thermoelectric Properties

Figure 4 shows the temperature-dependent curves of ρ, S, and power factor (PF) for $RECoO_3$ ceramics. The ρ-T curves varied from 300 K to 973 K, as shown in Figure 4a, demonstrating the low resistivity of all samples. LNSB and LNSBC show metallic conductive behaviors with the lowest resistivity of only 2.25 mΩ cm at 973 K, while LSBC has higher resistivity and exhibits a semiconductor–metal transition at around 650 K. Furthermore, the room-temperature carrier concentration (n) and carrier mobility (μ_H) were also obtained by testing the Hall effect. As listed in Table 1, LNSB is of the highest n of 6.7×10^{20} cm^{-3} compared with LNSBC (3.57×10^{20} cm^{-3}) and LSBC (1.06×10^{20} cm^{-3}), which could be attributed to the high average valence state (V_{RE}~2.5) originating from the introduction of more trivalent ions in the RE site of LNSB. However, the μ_{Hs} of the three samples showed the opposite trend (LSBC > LNSBC > LNSB); this may be because of the fewer grain boundaries in LSBC reducing carrier scattering and promoting the carrier's transport.

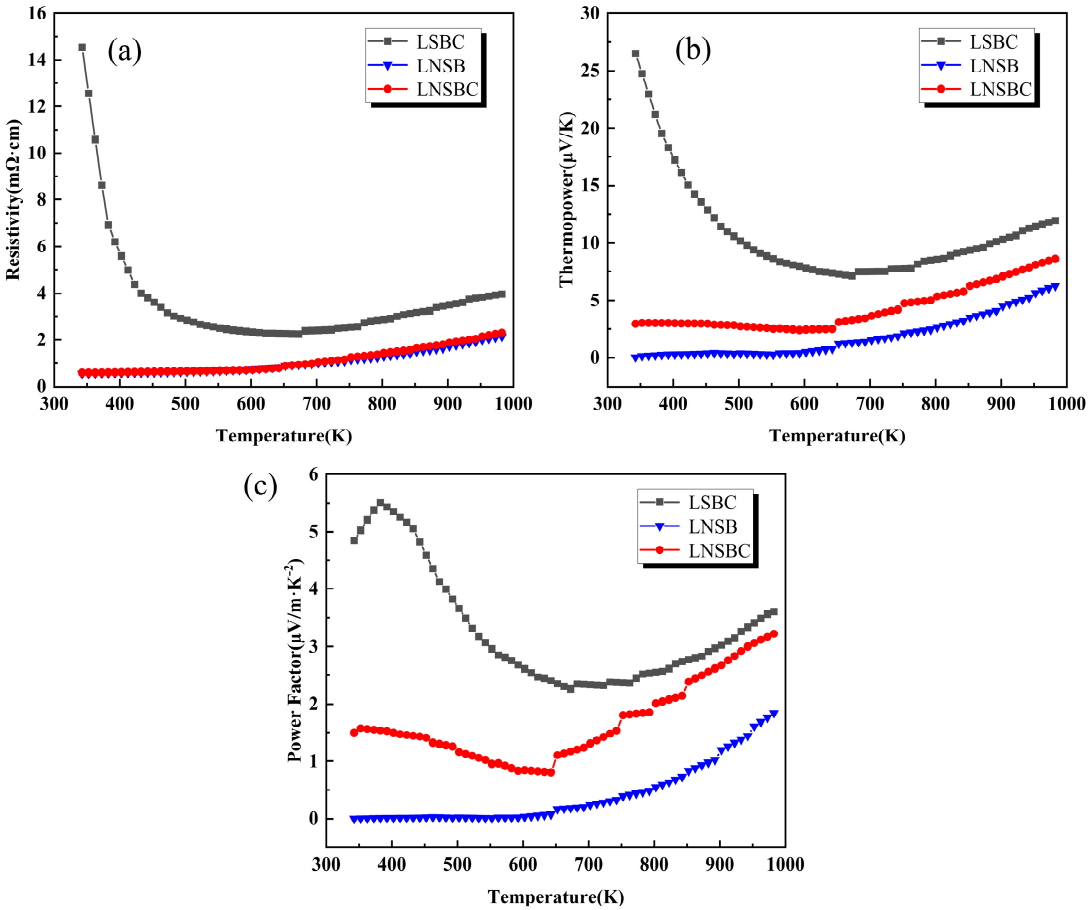


Figure 4. Temperature dependence of the electrical properties of high-entropy $RECoO_3$ ceramics. (**a**) Electrical resistivity (ρ). (**b**) Seebeck coefficient (S). (**c**) Power factor (PF).

Figure 4b shows the S-T curves of the three samples. The positive S values suggest that they are P-type thermoelectric materials. It can also be observed that LNSB and LNSBC, in terms of S, display a slow increase with increasing temperature, while LSBC decreases firstly and then increases, achieving the largest S of 27 $\mu V \cdot K^{-1}$ at 300 K. As a result, LSBC obtains a larger PF of 5.5 $\mu V/m \cdot K^{-2}$ at about 400 K compared with the other two samples (Figure 4c). We conclude that the low PF is suppressed by their high electrical properties and high carrier concentrations. In addition, when the temperature is higher than 650 K, the PF shows an upward trend. This is due to, on one hand, the spin state of Co ions

varying with the temperature, which will affect the *S* value [36,37]; on the other hand, the lattice oxygen may be volatilized at this temperature, in which the oxygen vacancies are formed to counteract the hole carrier, and show an increase in ρ and *S*. These behaviors have also been reported in the rare earth perovskite cobaltite [38,39].

Due to the V_{RE} of the RE site in $RECoO_3$ being closely associated with the chemical valences of Co ions as well as the TE properties, we therefore obtained the high-resolution Co 2p XPS spectrum of the LSBC, LNSB, and LNSBC samples. As shown in Figure 5, two major spin orbit peaks, Co $2p_{3/2}$ and Co $2p_{1/2}$, were observed, located at the binding energies of about 780.4 eV and 795.5 eV, respectively, which is in good agreement with the reported results [8]. Furthermore, the binding energies of ~798/794 eV and 780/795 eV should correspond to Co^{3+} and Co^{4+} and show hardly any obvious changes in the three samples. On the other hand, considering the influence of the spin entropy of Co ions (Co^{3+} and Co^{4+}) in the Co-based samples on TE performance, we further obtained the respective ratios of Co^{3+} and Co^{4+} by fitting the two main peaks and found that the three samples have a relatively high proportion of Co^{4+}. According to the modified Heikes rule [40], such a high concentration of Co^{4+} may result in a decrease in *S* values compared with similar Co-based perovskite oxides [12,13]. Notably, LSBC has the largest proportion of Co^{4+} (64.22%) compared with that of LNSB (59.41%) and LNSBC (62.30%). This is possibly due to the low V_{RE} in the RE site of LSBC resulting in more Co^{3+} transforming into Co^{4+} to meet the charge neutrality of the entire compound. Moreover, since such perovskite $RECoO_3$ samples often exhibit an oxygen vacancy phenomenon, which has a direct impact on the valence state of Co ions as well as the TE properties of materials, this complex relationship and influence mechanism between them is difficult to understand at present, with more experimental evidence being needed in future studies.

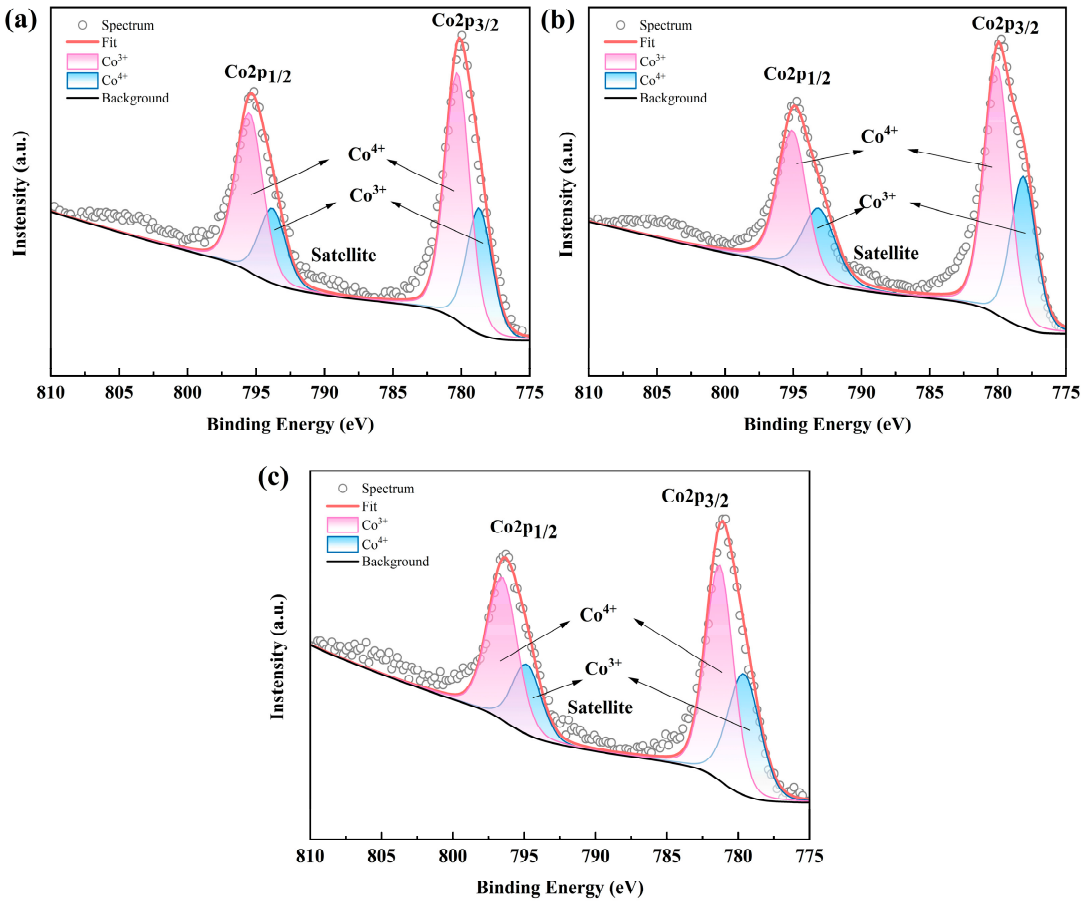


Figure 5. High-resolution Co 2p XPS spectra of (**a**) LSBC, (**b**) LNSB, and (**c**) LNSBC.

Figure 6 illustrates the thermal diffusion (D), total thermal conductivity (κ_{tot}), electron thermal conductivity (κ_e), and lattice thermal conductivity (κ_l) of the high-entropy $RECoO_3$ ceramics. It can be seen from Figure 5a that the three samples have maximum D coefficients of around 600 K. The inset shows the heat capacities (C_{ps}) of the three samples calculated from Cope's law [41], showing linear growth as the temperature rises. Figure 5b describes the variation curves between the κ_{tot} and temperature. It can be seen that LNSB and LNSBC have nearly the same κ_{tot} over the entire temperature range, yielding a maximum value of 2.4 $W \cdot m^{-1} \cdot K^{-1}$ at 600 K. However, the κ_{tot} of LSBC is lower than that of LNSB and LNSBC, and the lowest κ_{tot} of 1.25 $W \cdot m^{-1} \cdot K^{-1}$ at 973 K was obtained, which is far smaller than that of the similar $La_{0.95}Sr_{0.05}CoO_3$ (4 $W \cdot m^{-1} \cdot K^{-1}$) [42,43]. These findings signify that high-entropy design in RE sites effectively reduces thermal conductivity. To further analyze the changes in the thermal conductivity of the three samples, the κ_e was also calculated using the Wiedemann–Franz law [44] and then κ_l was obtained by abstracting the κ_e from the κ_{tot}. As depicted in Figure 6c, LNSB and LNSBC are dominated by κ_e due to their high conductivities, leading to a low κ_l over the entire temperature range (0.4~0.6 W m^{-1} K^{-1}). In contrast, LSBC is dominated by a κ_l below 600 K; as the temperature goes up, κ_l and κ_e contribute equally. In addition, it can be seen from the SEM mappings that the LSBC sample has large grain growth and low porosity, which can promote phonon transport between the grains and thus contribute to the relatively high κ_l. Moreover, the κ_e shows a transition near 600 K, since part of the lattice oxygen begins to volatilize at this temperature, resulting in a reduction in carrier concentration. Notably, compared with $La_{0.95}Sr_{0.05}CoO_3$, the κ_{es} of the three samples is significantly reduced, providing strong evidence that high-entropy effects in the RE site cause phonon scattering and greatly reduce the κ_e of the sample [45,46]. Although the high-entropy effect of the RE position can effectively inhibit the thermal conductivity of perovskite $RECoO_3$ materials, it is crucial to realize high PF or ZT values for future applications by increasing their Seebeck coefficients. We conclude that this part of the work can be achieved by further adjusting the chemical composition of multi-component cations to obtain balanced electrical conductivity and thermal conductivity.

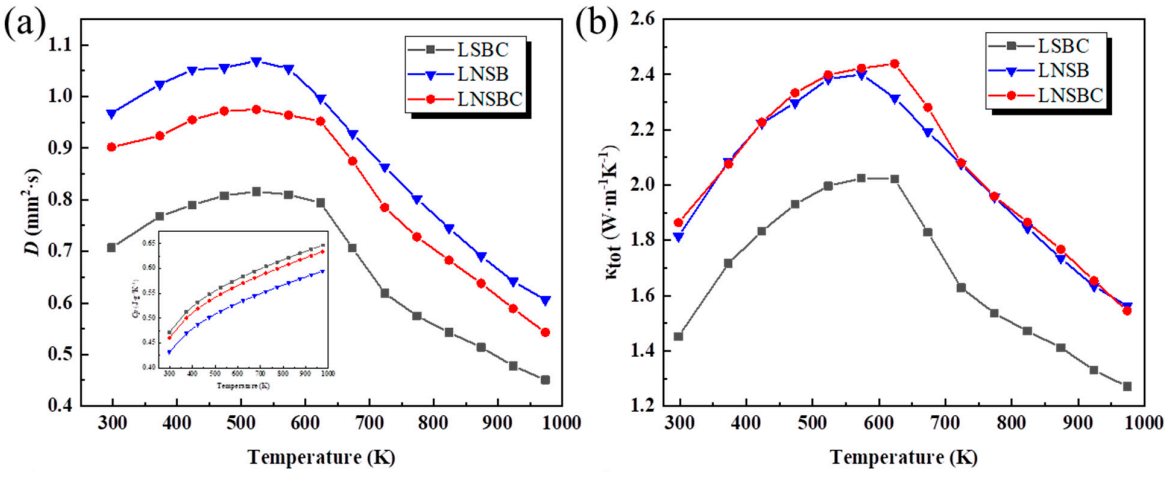


Figure 6. *Cont.*

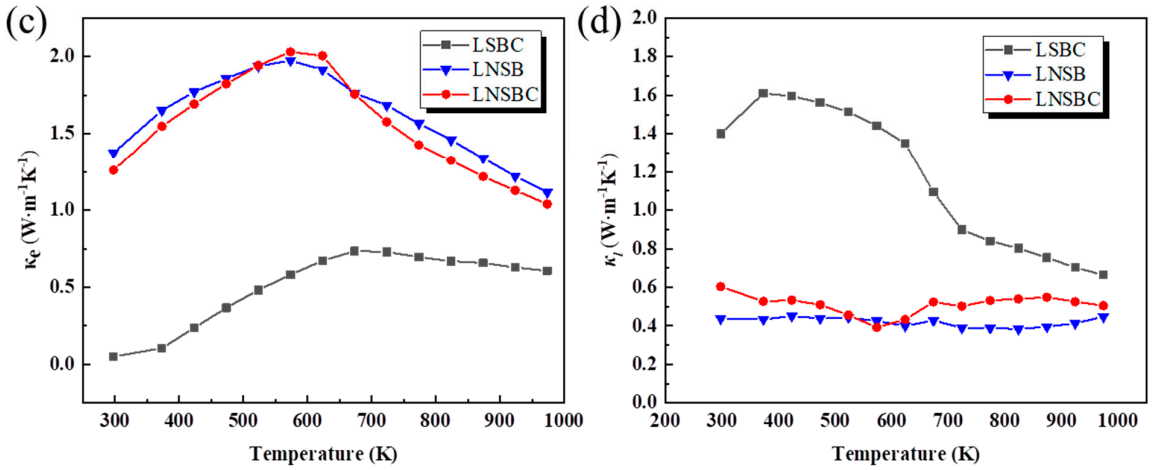


Figure 6. Temperature dependence of the thermal transport properties of the high-entropy $RECoO_3$ ceramics. (**a**) Thermal diffusion coefficients (D); the inset is the specific heating capacity (C_p). (**b**) Total thermal conductivity (κ_{tot}). (**c**) Electron thermal conductivity (κ_e). (**d**) Lattice thermal conductivity (κ_l).

4. Conclusions

In summary, we report a series of high-entropy $RECoO_3$ ceramics (LSBC, LNSB, and LNSBC) produced by introducing multi-component elements into the RE site, with the aim of regulating their electrical and thermal transport properties. All samples exhibited a uniform distribution of elements without phase segregation and element aggregation. The electrical transport measurements showed that, due to the increasing average valence state in the RE site cations, LNSB and LNSBC showed metallic conducting behaviors with excellent electrical properties, while LSBC exhibited a semiconductor–metal transition. In addition, these high-entropy ceramics show a high proportion of Co^{4+} for the requirement of charge neutrality in the samples due to the low average chemical valences, which inhibits their Seebeck coefficients. The thermal transport measurements showed that LSBC is dominated by lattice thermal conductivity, and the lowest thermal conductivity is about 1.25 W·m^{-1}·K^{-1} (937 K). In contrast, LNSB and LNSBC are dominated by electronic thermal conductivity, exhibiting a thermal conductivity of 1.52 W·m^{-1}·K^{-1} at the same temperature. This suggests that the lattice distortion resulting from RE site disorder forms multi-scale phonon scattering centers and inhibits the lattice thermal conductivity, whereas increasing the V_{RE} of cations can enhance electronic thermal conductivity. These results show that the entropy engineering strategy can effectively regulate the electrical and thermal transport properties or behaviors of thermoelectric materials and induce some novel physical phenomena.

Author Contributions: K.Z.: Writing—original draft, Methodology, Investigation, Formal analysis, Data curation, Conceptualization. C.Y.: Investigation, Conceptualization, Formal analysis. X.A.: Investigation, Methodology. Y.Z.: Investigation. W.T.: Investigation. J.W.: Investigation. B.L.: Writing—review & editing, Supervision, Resources, Project administration, Methodology, Investigation, Funding acquisition, Conceptualization. K.D.: Software. L.C.: Software. L.Y.: Supervision, Resources, Writing—review & editing. All authors have read and agreed to the published version of the manuscript.

Funding: This work was supported by the Yunnan Fundamental Research Projects (202201AU070118, 202401AT070378) and the Analysis and Testing Foundation of Kunming University of Science and Technology.

Data Availability Statement: Data will be made available on request.

Acknowledgments: We acknowledge the financial support by the Yunnan Fundamental Research Projects and the Analysis and Testing Foundation of Kunming University of Science and Technology.

Conflicts of Interest: The authors declare no conflict of interest.

References

1. Snyder, G.J.; Toberer, E.S. Complex thermoelectric materials. *Nat. Mater.* **2008**, *7*, 105–114. [CrossRef] [PubMed]
2. Nie, G.; Li, W.; Guo, J.; Yamamoto, A.; Kimura, K.; Zhang, X.; Isaacs, E.B.; Dravid, V.; Wolverton, C.; Kanatzidis, M.G.; et al. High-Performance Thermoelectric Module through Isotype Bulk Heterojunction Engineering of Skutterudite Materials. *Nano Energy* **2019**, *66*, 104193. [CrossRef]
3. Mukherjee, M.; Srivastava, A.; Singh, A.K. Recent advances in designing thermoelectric materials. *J. Mater. Chem. C* **2022**, *10*, 12524–12555. [CrossRef]
4. Han, Z.; Li, J.W.; Jiang, F.; Xia, J.; Zhang, B.P.; Li, J.F.; Liu, W. Room-temperature thermoelectric materials: Challenges and a new paradigm. *J. Mater.* **2022**, *8*, 427–436. [CrossRef]
5. Jia, S.; Qian, W.; Yu, P.; Li, K.; Li, M.; Lan, J.; Lin, Y.-H.; Yang, X. Ionic thermoelectric materials: Innovations and challenges. *Mat. Today Phys.* **2024**, *42*, 101375. [CrossRef]
6. Ge, B.; Li, R.; Wang, G.; Zhu, M.; Zhou, C. Oxide semiconductors for thermoelectric: The challenges and future. *J. Am. Chem. Soc.* **2024**, *107*, 1985–1995. [CrossRef]
7. Snyder, G.J.; Christensen, M.; Nishibori, E.; Caillat, T.; Iversen, B.B. Disordered zinc in Zn_4Sb_3 with phonon-glass and electron-crystal thermoelectric properties. *Nat. Mater.* **2004**, *3*, 458–463. [CrossRef]
8. Yang, C.; Wu, H.; Song, H.; Wang, X.; Chen, S.; Xu, X.; Chen, L.; Zhao, Z.; Yu, L.; Liu, B. Ultralow thermal conductivity and enhanced thermoelectric properties in a textured $(Ca_{0.35}Sr_{0.2}Ba_{0.15}Na_{0.2}Bi_{0.1})3Co_4O_9$ high-entropy ceramic. *J. Alloy. Compd.* **2023**, *940*, 168802. [CrossRef]
9. Hébert, S.; Flahaut, D.; Martin, C.; Lemonnier, S.; Noudem, J.; Goupil, C.; Maignan, A.; Hejtmanek, J. Thermoelectric properties of perovskites: Sign change of the Seebeck coefficient and high temperature properties. *Prog. Solid State Chem.* **2007**, *35*, 457–467. [CrossRef]
10. Wu, T.; Gao, P. Development of perovskite-type materials for thermoelectric application. *Materials* **2018**, *11*, 999. [CrossRef]
11. Fergus, J.W. Oxide materials for high temperature thermoelectric energy conversion. *J. Eur. Ceram. Soc.* **2012**, *32*, 525–540. [CrossRef]
12. Bousnina, M.A.; Dujardin, R.; Perriere, L.; Giovannelli, F.; Guegan, G.; Delorme, F. Synthesis, sintering, and thermoelectric properties of the solid solution $La_{1-x}Sr_x\ CoO_{3\pm\delta}$ ($0 \leq x \leq 1$). *J. Adv. Ceram.* **2018**, *7*, 160–168. [CrossRef]
13. Wang, Y.; Sui, Y.; Ren, P.; Wang, L.; Wang, X.; Su, W.; Fan, H.J. Correlation between the Structural Distortions and Thermoelectric Characteristics in $La_{1-x}A_xCoO_3$ (A=Ca and Sr). *Inorg. Chem.* **2010**, *49*, 3216–3223. [CrossRef] [PubMed]
14. Robert, R.; Aguirre, M.H.; Bocher, L.; Trottmann, M.; Heiroth, S.; Lippert, T.; Doebeli, M.; Weidenkaff, A. Thermoelectric properties of $LaCo_{1-x}Ni_xO_3$ polycrystalline samples and epitaxial thin films. *Solid State Sci.* **2008**, *10*, 502–507. [CrossRef]
15. Jiamprasertboon, A.; Okamoto, Y.; Hiroi, Z.; Siritanon, T. Thermoelectric properties of Sr and Mg double-substituted $LaCoO_3$ at room temperature. *Ceram. Int.* **2014**, *40*, 12729–12735. [CrossRef]
16. Kumar, A.; Sivaprahsam, D.; Thakur, A.D. Improvement of thermoelectric properties of lanthanum cobaltate by Sr and Mn co-substitution. *J. Alloy. Compd.* **2018**, *735*, 1787–1791. [CrossRef]
17. Lou, Z.; Zhang, P.; Zhu, J.; Gong, L.; Xu, J.; Chen, Q.; Reece, M.J.; Yan, H.; Gao, F. A novel high-entropy perovskite ceramics $Sr_{0.9}La_{0.1}(Zr_{0.25}Sn_{0.25}Ti_{0.25}Hf_{0.25})O_3$ with low thermal conductivity and high Seebeck coefficient. *J. Eur. Ceram. Soc.* **2022**, *42*, 3480–3488. [CrossRef]
18. Messing, G.L.; Poterala, S.; Chang, Y.; Frueh, T.; Kupp, E.R.; Watson, B.H., III; Walton, R.L.; Brova, M.J.; Hofer, A.-K.; Bermejo, R.; et al. Texture-engineered ceramics-Property enhancements through crystallographic tailoring. *J. Mater. Res.* **2017**, *32*, 3219–3241. [CrossRef]
19. Torres, M.; Costa, F.; Flahaut, D.; Touati, K.; Rasekh, S.; Ferreira, N.; Allouche, J.; Depriester, M.; Madre, M.; Kovalevsky, A.V.; et al. Significant enhancement of the thermoelectric performance in $Ca_3Co_4O_9$ thermoelectric materials through combined strontium substitution and hot-pressing process. *J. Eur. Ceram. Soc.* **2019**, *39*, 1186–1192. [CrossRef]
20. Noudem, J.G. A new process for lamellar texturing of thermoelectric $Ca_3Co_4O_9$ oxides by spark plasma sintering. *J. Eur. Ceram. Soc.* **2009**, *29*, 2659–2663. [CrossRef]
21. Miracle, D.B.; Senkov, O.N. A critical review of high entropy alloys and related concepts. *Acta Mater.* **2017**, *122*, 448. [CrossRef]
22. George, E.P.; Raabe, D.; Ritchie, R.O. High-entropy alloys. *Nat. Rev. Mater.* **2019**, *4*, 515. [CrossRef]
23. Oses, C.; Toher, C.; Curtarolo, S. High-entropy ceramics. *Nat. Rev. Mater.* **2020**, *5*, 295–309. [CrossRef]
24. Liu, B.; Wu, J.; Cui, Y.; Zhu, Q.; Xiao, G.; Wu, S.; Cao, G.H.; Ren, Z. Structural evolution and superconductivity tuned by valence electron concentration in the Nb-Mo-Re-Ru-Rh high-entropy alloys. *J. Mater. Sci. Technol.* **2021**, *85*, 11. [CrossRef]

25. Luo, Y.; Hao, S.; Cai, S.; Slade, T.J.; Luo, Z.Z.; Dravid, V.P.; Wolverton, C.; Yan, Q.; Kanatzidis, M.G. High Thermoelectric Performance in the New Cubic Semiconductor $AgSnSbSe_3$ by High-Entropy Engineering. *J. Am. Chem. Soc.* **2020**, *142*, 15187. [CrossRef] [PubMed]
26. Jiang, B.; Yu, Y.; Cui, J.; Liu, X.; Xie, L.; Liao, J.; Zhang, Q.; Huang, Y.; Ning, S.; Jia, B.; et al. High-Entropy-Stabilized Chalcogenides with High Thermoelectric Performance. *Science* **2021**, *371*, 830. [CrossRef]
27. Zheng, Y.; Zou, M.; Zhang, W.; Yi, D.; Lan, J.; Nan, C.-W.; Lin, Y.-H. Electrical and Thermal Transport Behaviours of High-Entropy Perovskite Thermoelectric Oxides. *J. Adv. Ceram.* **2021**, *10*, 377. [CrossRef]
28. Zhang, M.; Cai, J.; Gao, F.; Zhang, Z.; Li, M.; Chen, Z.; Wang, Y.; Hu, D.; Tan, X.; Liu, G.; et al. Improved Thermoelectric Performance of P-Type PbTe by Entropy Engineering and Temperature-Dependent Precipitates. *ACS Appl. Mater. Interfaces* **2024**, *16*, 907. [CrossRef]
29. Gao, H.; Zhao, K.; Wuliji, H.; Zhu, M.; Xu, B.; Lin, H.; Fei, L.; Zhang, H.; Zhou, Z.; Lei, J.; et al. Adaptable Sublattice Stabilized High-Entropy Materials with Superior Thermoelectric Performance. *Energy Environ. Sci.* **2023**, *16*, 6046. [CrossRef]
30. Xu, X.; Yang, W.Z.; Song, H.Y.; Wang, J.S.; Yu, L.; Ren, Z.; Liu, B. Structural sequence and superconductivity in high-entropy Mo-W-Re-Ru-Pd alloys. *Scr. Mater.* **2024**, *243*, 115986. [CrossRef]
31. Liu, R.; Chen, H.; Zhao, K.; Qin, Y.; Jiang, B.; Zhang, T.; Sha, G.; Shi, X.; Uher, C.; Zhang, W.; et al. Entropy as a Gene-Like Performance Indicator Promoting Thermoelectric Materials. *Adv. Mater.* **2017**, *29*, 1702712. [CrossRef] [PubMed]
32. Liu, B.; Yang, W.; Xiao, G.; Zhu, Q.; Song, S.; Cao, G.H.; Ren, Z. High-entropy silicide superconductors with W_5Si_3-type structure. *Phys. Rev. Mater.* **2023**, *7*, 014805.
33. Rahaman, M.D.; Mia, M.D.; Khan, M.N.I.; Hossain, A.A. Study the effect of sintering temperature on structural, microstructural and electromagnetic properties of 10% Ca-doped $Mn_{0.6}Zn_{0.4}Fe_2O_4$. *J. Magn. Magn. Mater.* **2016**, *404*, 238–249. [CrossRef]
34. Kharton, V.V.; Tsipis, E.V.; Yaremchenko, A.A.; Marozau, I.P.; Viskup, A.P.; Frade, J.R.; Naumovich, E.N. Oxygen permeability, electronic conductivity and stability of $La_{0.3}Sr_{0.7}CoO_3$-based perovskites. *Mat. Sci. Eng. B* **2006**, *134*, 80–88. [CrossRef]
35. Ma, Z.; Xu, T.; Li, W.; Cheng, Y.; Li, J.; Zhang, D.; Jiang, Q.; Luo, Y.; Yang, J. High entropy semiconductor $AgMnGeSbTe_4$ with desirable thermoelectric performance. *Adv. Funct. Mater.* **2021**, *31*, 2103197. [CrossRef]
36. Terasaki, I.; Sasago, Y.; Uchinokura, K. Large thermoelectric power in $NaCo_2O_4$ single crystals. *Phys. Rev. B* **1997**, *56*, R12685. [CrossRef]
37. Liu, Y.; Zhang, L.; Shirsath, S.E.; Zheng, J.; Liu, Y.; Ulrich, C.; Li, S. Manipulation of charge carrier concentration and phonon scattering via spin-entropy and size effects: Investigation of thermoelectric transport properties in La-doped $Ca_3Co_4O_9$. *J. Alloy. Compd.* **2019**, *801*, 60–69. [CrossRef]
38. Kumar, A.; Dragoe, D.; Berardan, D.; Dragoe, N. Thermoelectric properties of high-entropy rare-earth cobaltates. *J. Mater.* **2023**, *9*, 191–196. [CrossRef]
39. Kotiuga, M.; Zhang, Z.; Li, J.; Rodolakis, F.; Zhou, H.; Sutarto, R.; He, F.; Wang, Q.; Sun, Y.; Wang, Y.; et al. Carrier localization in perovskite nickelates from oxygen vacancies. *Proc. Natl. Acad. Sci. USA* **2019**, *116*, 21992–21997. [CrossRef]
40. Sparks, T.D.; Gurlo, A.; Gaultois, M.W.; Clarke, D.R. Revised model for thermopower and site inversion in Co_3O_4 spinel. *Phys. Rev. B* **2018**, *98*, 024108. [CrossRef]
41. Alroy, J. Cope's rule and the dynamics of body mass evolution in North American fossil mammals. *Science* **1998**, *280*, 731–734. [CrossRef] [PubMed]
42. Zhang, X.; Li, X.M.; Chen, T.L.; Chen, L.D. Thermoelectric and transport properties of $La_{0.95}S_{r0.05}CoO_3$. *J. Cryst. Growth* **2006**, *286*, 1–5. [CrossRef]
43. Androulakis, J.; Migiakis, P.; Giapintzakis, J. $La_{0.95}Sr_{0.05}CoO_3$: An efficient room-temperature thermoelectric oxide. *Appl. Phys. Lett.* **2004**, *84*, 1099–1101. [CrossRef]
44. Hu, Y.D.; Li, Y.; Wu, H.R.; Tang, Y.Y.; Fan, K.; Liu, B.; Yu, L. Laser-induced transverse voltage effect in *c*-axis inclined $CuCr_{0.98}Mg_{0.02}O_2$ thin films with dominant phonon thermal conductivity. *J. Appl. Phys.* **2021**, *130*, 143104. [CrossRef]
45. Liu, X.; Zhang, P.; Huang, M.; Han, Y.; Xu, N.; Li, Y.; Zhang, Z.; Pan, W.; Wan, C. Effect of lattice distortion in high-entropy $RE_2Si_2O_7$ and RE_2SiO_5 (RE= Ho, Er, Y, Yb, and Sc) on their thermal conductivity: Experimental and molecular dynamic simulation study. *J. Eur. Ceram. Soc.* **2023**, *43*, 6407–6415. [CrossRef]
46. Körmann, F.; Ikeda, Y.; Grabowski, B.; Sluiter, M.H. Phonon broadening in high entropy alloys. *npj Comput. Mater.* **2017**, *3*, 36. [CrossRef]

Disclaimer/Publisher's Note: The statements, opinions and data contained in all publications are solely those of the individual author(s) and contributor(s) and not of MDPI and/or the editor(s). MDPI and/or the editor(s) disclaim responsibility for any injury to people or property resulting from any ideas, methods, instructions or products referred to in the content.